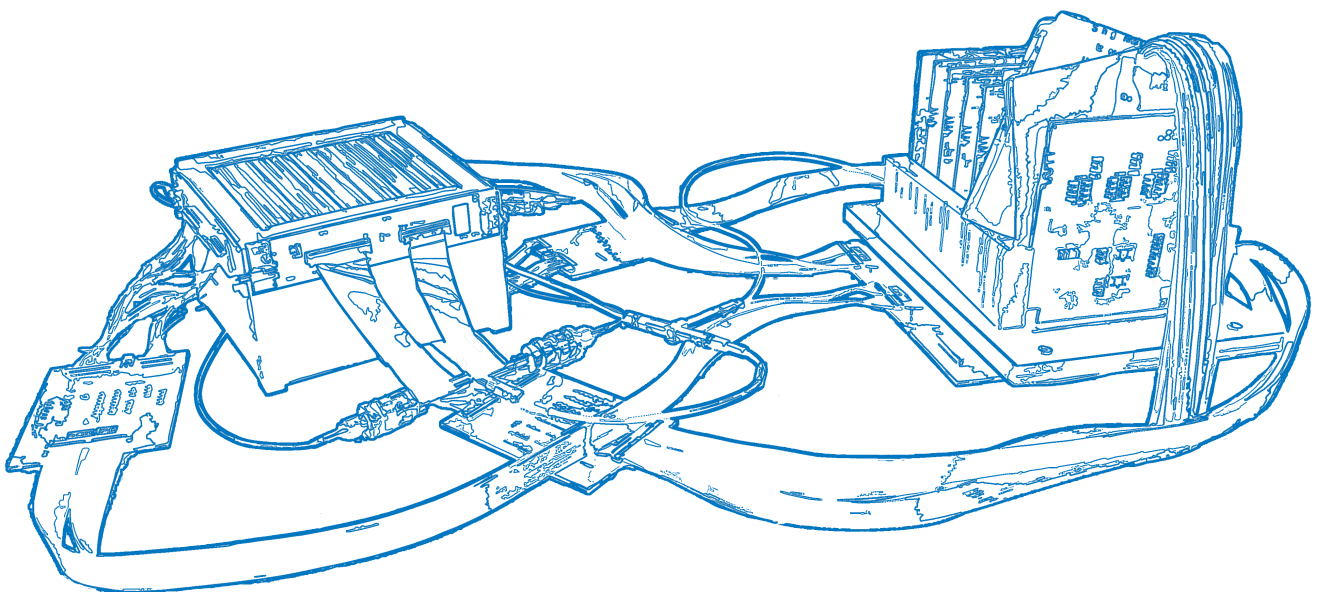Technische Universität München
Fakultät für Physik

Abschlussarbeit im Bachelorstudiengang Physik

Development of a Trigger System with a Cosmic Muon Tracker

Entwicklung und Aufbau eines Triggerdetektors mit einem Tracker für Kosmische Myonen

Luis Hofbauer

11. Oktober 2021

Erstgutachter (Themensteller): Prof. L. Fabbietti
Zweitgutachter: PD Dr. Greiner.

Contents

Contents

List of Figures

Abstract

There is an ongoing effort in the development of gaseous detectors capable of detecting visible light. For the characterization and qualification of the first prototypes aiming to achieve this, a peripheral detector setup capable of advanced tracking and corresponding triggering is required. In this thesis, the first developments of such a detector are carried out, tested and studied.

To realise the setup, a preexisting detector featuring 256 scintillating fibers arranged into 8 orthogonal layers was used. The fibers are coupled to Silicon Photomultipliers which output a signal proportional to the scintillator light intensity.

For the readout, the DiRICH, which is a data acquisition and trigger system was implemented. It features time to digital converters which determine time stamps for the rising and falling edge of a signal at a certain threshold amplitude. With this, the time over threshold of a signal can be determined.

This setup was used to measure cosmic rays at sea level which consist of muons in the vast majority. Using the expected cosmic muon energy range, energy loss, and pion data for reference the measured time over threshold distribution was made plausible. By investigating particle coincidence between different layers of the detector cosmic particles could be clearly identified as part of the measured signal. Additionally, the first developments towards particle tracking through the detector have been made. To conclude significant developments towards a trigger and tracker system were successfully made establishing the prospect of its use in future experiments.

Chapter 1

Introduction

1.1 Motivation

A new gaseous detector capable of detecting visible light using a Gas Electron Multiplier (GEM) has been developed. In order to study and characterize this detector an external system for particle tracking and triggering is required to distinguish events deemed interesting from uninteresting ones.
GEMs are used in gaseous detectors to multiply initial electrons produced by an incoming particle ionizing the gas within the detector until an electron avalanche is formed. The general structure of a detector featuring a GEM is depicted in figure 1.1.
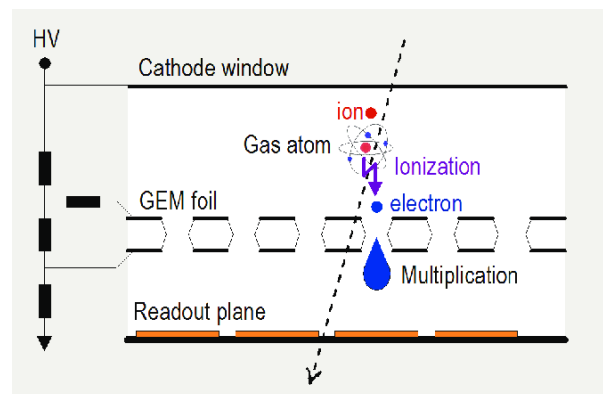
Figure 1.1: Illustration of gaseous ionization detector employing a GEM foil [1].

The GEM is a thin foil featuring an array of microscopic holes. Between the top and bottom of the foil a high voltage is applied thus creating a strong electric field inside and in close proximity of the hole. Here the electron multiplication takes places. The resulting avalanche is transmitted to an electronic readout.
The distinctive feature of the detector in question here is the coating of a photosensitive material on the top side of the foil which enables the capability to detect visible light. The detector is a photosensitive thick-GEM (photo-THGEM), where the prefix thick just means that the GEM foil has increased dimensions.
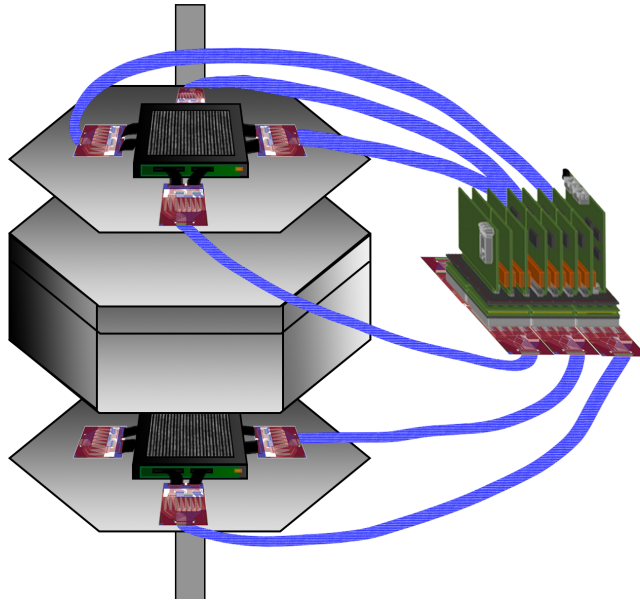
Figure 1.2: Schematic view of the fully assembled detector setup. The photo-THGEM is placed between the fiber detectors which connected to the DiRICH on the right. Graphic by Berkin Ulukutlu.

As mentioned above in order to first characterize the photo-THGEM detector an external system capable of particle tracking and subsequent triggering is needed. This peripheral detector setup will use two scintillating fiber detectors, placed above and below the photo-THGEM. These scintillation detectors were originally developed for the RadMap [2] telescope. They feature 256 scintillating plastic fibers arranged in 8 layers. Each of the fibers is connected to an individual Silicon Photomultiplier (SiPM). This structure enables advanced particle tracking through the setup depicted in figure 1.2.

As a proof of principle the entire setup will be used first to measure cosmic particles. In order to identify cosmic particles from background β-particles, particle tracking is necessary. Identifying cosmic particles by tracking is possible because β-particles are not trackable as they are very likely to be scattered out of a straight path or to be absorbed in the scintillator. The reason is that the energy range of β-particles is much lower, in the tens of keV to a few MeV [3], than the energy range of cosmic muons which starts at a couple hundred MeV (see figures 1.4 and 1.3).

When a cosmic particle has been identified a corresponding trigger signal will be generated and forwarded to the photo-THGEM readout. For this the DiRICH data acquisition and trigger system will be used. Furthermore the DiRICH handles the

readout of the fiber scintillator detectors. During this thesis the fiber detectors with the corresponding DiRICH readout are implemented and tested. Furthermore, first developments towards tracking are made.

1.2 Cosmic rays

Aiming to introduce cosmic rays, firstly one has to differentiate between primary and secondary cosmic rays. Primary cosmic rays originate from the sun, the milky-way or extragalactic sources [4]. Upon entering the earths atmosphere they react with surrounding nuclei leading to showers of secondary particles (secondary cosmic rays). Primary cosmic rays are high energy particles whereby they are comprised mostly of atomic nuclei and electrons by a small part. Of the nuclei 90% are protons, 9% alpha particles and 1% heavier nuclei [5]. In the reaction of the primary particles with atmospheric nuclei a variety of hadrons most of which are pions but also other mesons and baryons are produced. The mesons are not stable and decay further, for instance neutral pions preferably decay into two gamma rays causing electrons and positrons to form in an electromagnetic cascade. On the other hand charged pions preferably decay into a muons and neutrinos, typically high in the atmosphere at about 15km altitude [6].

At sea level, cosmic muons have the highest flux (see figure 1.5) of any particle type by far with about $70 \, \mathrm{m}^{-2}\mathrm{s}^{-1}\mathrm{sr}^{-1}$ vertical flux which translates to about $1 \, \mathrm{cm}^{-2}\mathrm{min}^{-1}$ [6]. Figures 1.3 and 1.4 show the cosmic muon energy distribution for high and low energies respectively. The distribution rises from low energies at $300 \, \mathrm{MeV}$ where the CAPRICE measurements start to a peak at $1 \, \mathrm{GeV}$ and reaches much higher energies but with heavily decreasing fluxes.

For this thesis all measurements were conducted in the TUM physics department in Garching. Consequently, cosmic particles have to cross multiple thick layers of steel-reinforced concrete before reaching the detector setup. As a result only cosmic muons in the MIP range are expected to be observed. This can be explained by looking at the energy loss plot which rises sharply below MIP (minimum ionizing particle) energy (see figure 1.6). Thus cosmic muons reaching an energy below the MIP range while moving through the building are quickly absorbed or lose the vast amount of their energy, making them indistinguishable from background radiation.
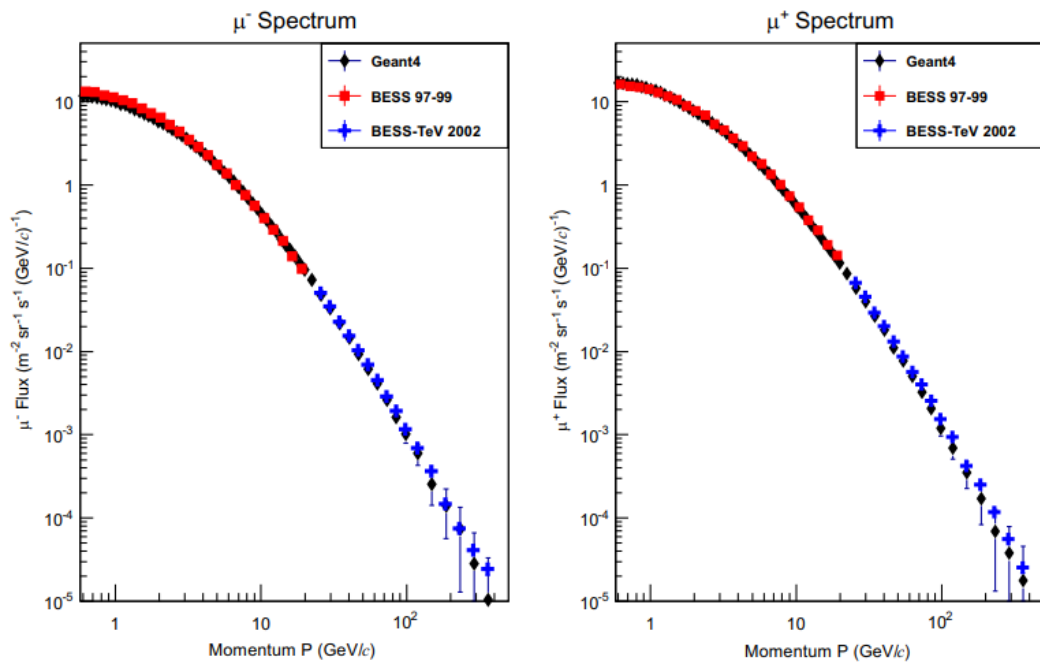
Figure 1.3: Differential momentum distribution for vertical cosmic muons at sea level, with negative muons on the left and positive on the right [7].
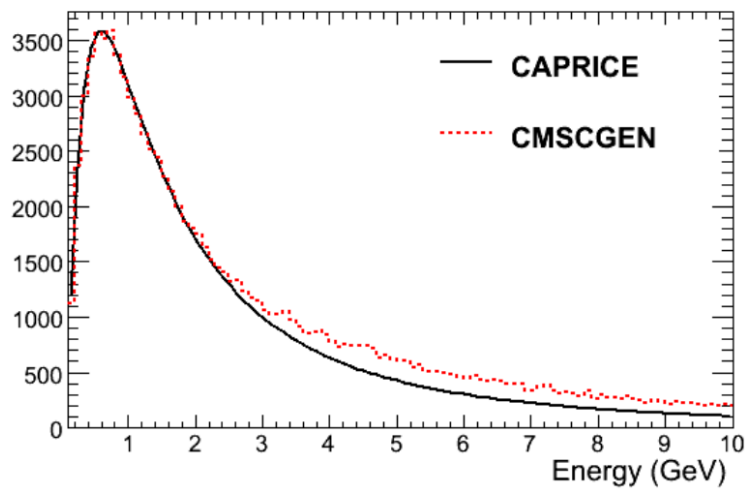
Figure 1.4: Results for cosmic muon energy distribution at low energies for the CAPRICE experiment and CMSCGEN simulation [8].
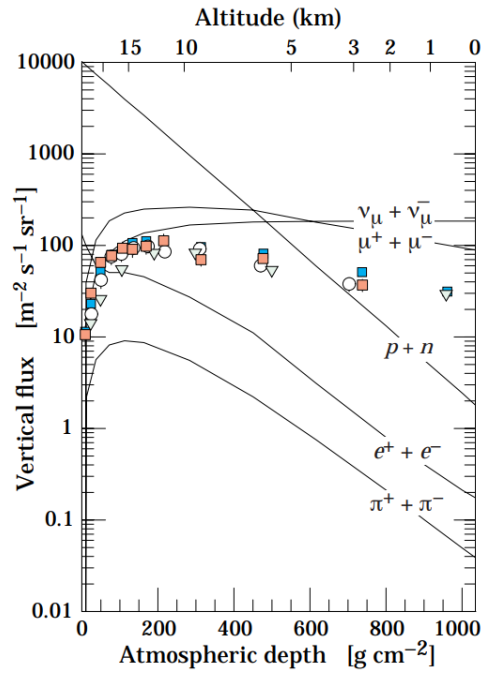
Figure 1.5: Estimated vertical cosmic radiation flux versus altitude for different particles [6].
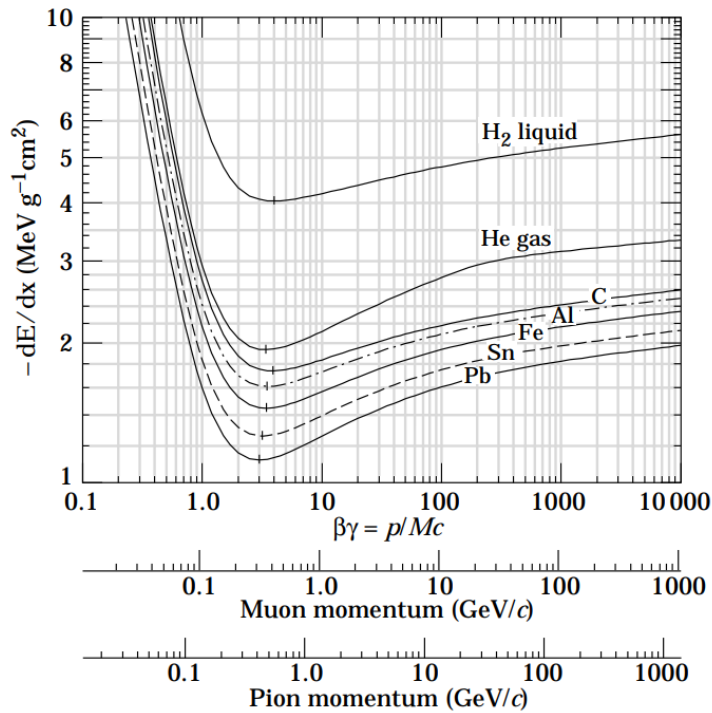
Figure 1.6: Bethe-Bloch energy loss versus $\beta\gamma$ for muons, pions and protons the minimum ionizing region normalized to density for different materials [9].

Chapter 2

DiRICH

For the RadMap project the scintillating fiber detectors were previously read out using a combination of Padiwas[10] and the TRB3[11] system. That specific setup, however, didn't provide enough channels to read out an entire detector. But as this is necessary to definitely reconstruct a track through the detector the system was replaced with the DiRICH system shown in figure 2.1. The DiRICH features 384 channels, enough to readout one and a half detectors.

Furthermore the DiRICH system, its parts and underlying working principles will be presented and explained.
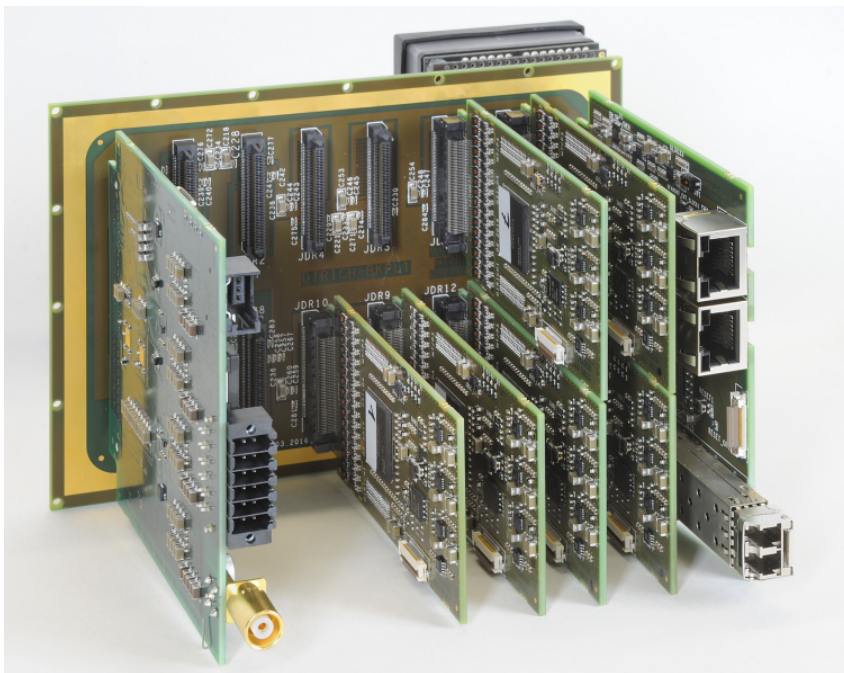
Figure 2.1: Picture of the DiRICH system with some front end boards not plugged in.
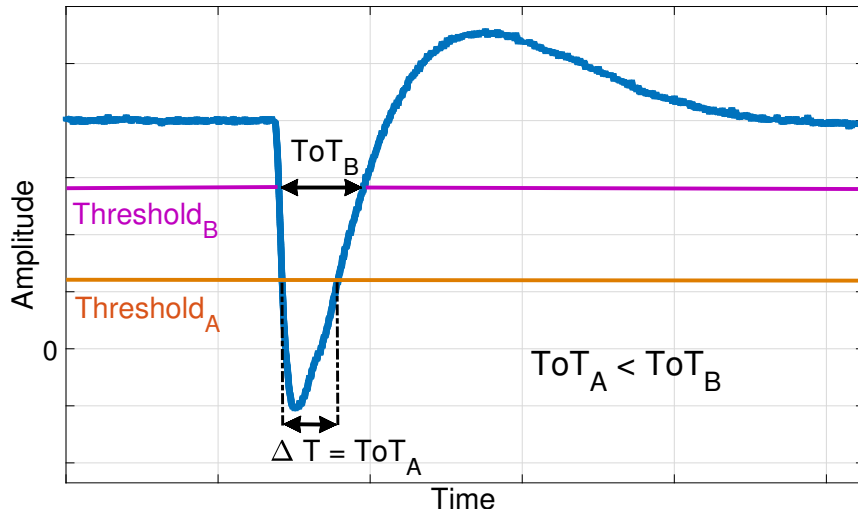
Figure 2.2: Schematic of the time over threshold for a negative output signal for two thresholds. The blue line depicts the filtered output signal from a single SiPM measured with an oscilloscope.

2.1 Time over threshold method

The ToT of a signal is determined by taking the difference of the rising and falling edge time stamps. In figure 2.2 a schematic of a filtered SiPM signal and with two for now arbitrary thresholds and their resulting ToTs is depicted. The x-axis represents time and the y-axis represents signal amplitude. This makes clear that at higher thresholds, considering the absolute the ToT will be lower. So in absolute terms $Threshold_A$ is larger than $Threshold_B$ and thus, because of the signal shape ToT_A is smaller than ToT_B.

The ToT directly only defines signal width while any other information, most notably the signal amplitude is lost initially. However the ToT is still proportional to the signal amplitude. Thus for a given signal shape and threshold the signal amplitude can be deduced from the ToT by introducing a conversion.

The usage of a ToT based readout also brings advantages with it. ToT measurements can be taken at a much higher rates and with better timing precision compared to ADC (analog-digital-converter) based systems. Additionally the dynamic range is theoretically limitless, meaning that no matter the size of the input signal it will always be recorded accurately, which is not the case for ADC measurements.

When measuring, the threshold has to be adjusted high enough so that signal can be distinguished from noise. As at a low threshold a signal with small slope and small amplitude i.e. noise can result in the same ToT as a high amplitude signal with steep

edges. But the thresholds also must not be set too high as otherwise parts of the signal may also be lost.

From the ToT of a signal the energy loss inside the detector by a particle can be obtained, if the signal is proportional to the energy loss and a ToT to energy conversion from a calibration is given.

2.2 DiRICH hardware components

The DiRICH consists of a variety of sub-units. The base of the DiRICH is formed by the backplane on which all sub-units are plugged in. Twelve frontend boards, with 32 channels each are responsible for the signal processing, time measurement and data acquisition. The frontend boards are numbered 1200, 1201, ...1209, 120a, 120b. All recorded data from the frontends is transmitted to the data concentrator, where it is combined into one coherent data package. Furthermore, the data concentrator holds the parts responsible for the communication of trigger signals for the internal readout to the frontends and their synchronization. The entire DiRICH is powered via the power board. The components of the DiRICH are more closely examined in the following.
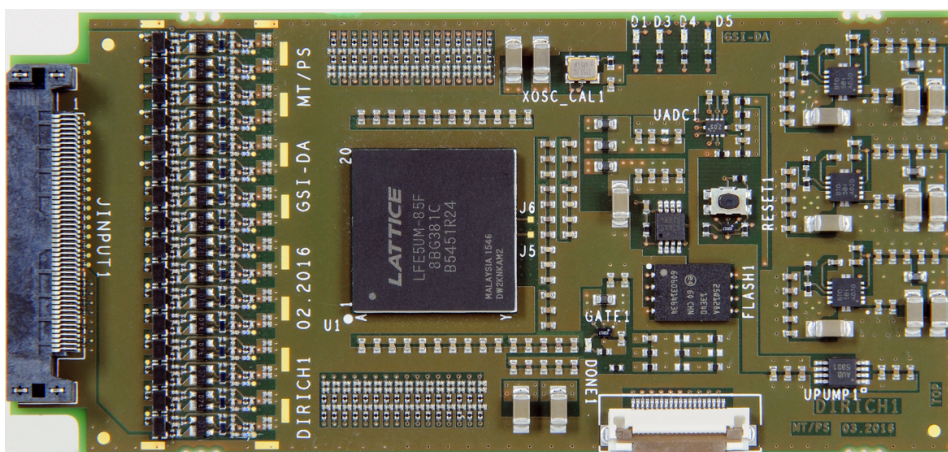
Figure 2.3: Picture of the DiRICH frontend readout board [12].

Frontends: The data acquisition as a whole takes place on the DiRICH frontend modules. Every board executes a variety of tasks which are mostly running on its central FPGA. Firstly, the time to digital converter (TDC) performs the actual time measurement with a 10 ps intrinsic time precision. Both the rising and falling edge of a pulse can be detected in the same channel, which is being achieved by stretching the falling edge of a pulse longer than the dead time of the channel caused by the

data acquisition such that the channel can be reused. This stretching of the pulse is carried out by the TDC enabling a single-channel ToT measurement.

Two peripheral FPGAs controlled by the central FPGA produce the signal thresholds for each channel which are then applied by the discriminator. Furthermore each channel features an amplifier (gain = 30) and a transformer.

Power board: Each DiRICH module is supplied with power from the power board, which offers two options to do so. To minimise noise one can use an external linear regulated power supply, feeding power to all electrical loads at their specific voltages from 1.1 V to 3.3 V. Hereby separate supply lines with no internal converters are used. As a relatively large current has to be applied the voltage drop over the cables can be quite large, potentially introducing stability issues if not taken care of. As an alternative one can use a 32 V single input which is routed to an on-board DC/DC converter producing all the needed voltages.

Additionally the power board offers a high voltage input connector, which can be used to power the scintillating fiber detectors (see section 3.2) used in the final setup and an internal clock, which is used as reference time .
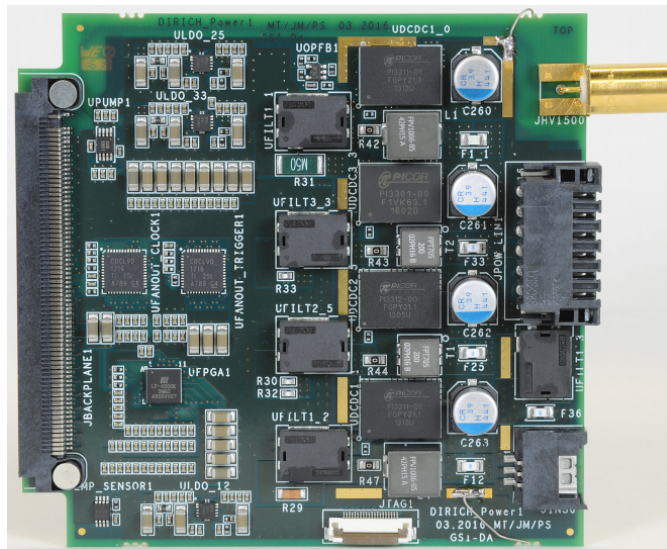
Figure 2.4: Picture of the DiRICH power board [12].

Data Concentrator: As the name suggests all extracted data from the frontends is sent to the Data Concentrator which subsequently merges the data into one packet. These data packets are then transported via the TRBNet link connector of the board to an event builder PC or server. In this way the Data Concentrator acts as the output for the data acquisition.

On its central FPGA the Central Triggering System (CTS), which is responsible for the decision over trigger signals and their distribution to the frontends (see section 2.4) is running. In addition connectors for external trigger and clock sources are provided on the board.
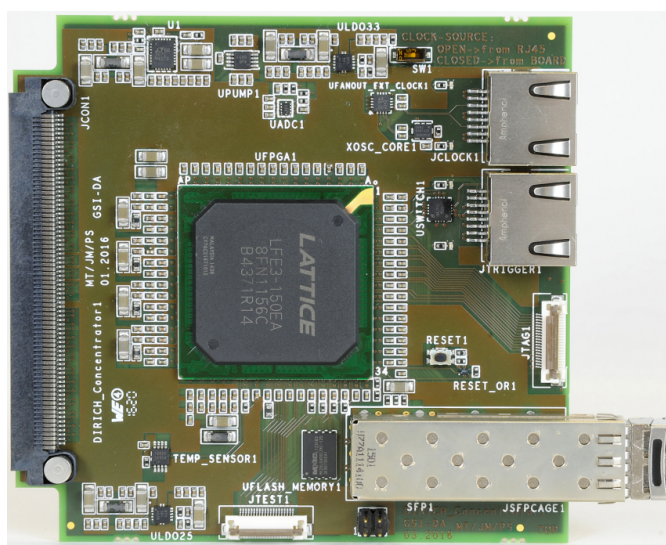
Figure 2.5: Picture of the DiRICH Data Concentrator [12].

2.3 Time to digital converter

In general TDCs (time to digital converters) are devices that measure timing information of signal i.e the time an event occurred and convert it to a digital output. On the DiRICH the TDCs are designed to recognise when a signal crosses a certain (for now arbitrary) threshold, the rising or leading edge, and when a signal falls below said threshold, the falling edge. A rising followed by a falling edge represents an event e.g. a cosmic muon passing trough the detector. The TDC determines the time stamps for both edges. Their difference provides the ToT of the signal, the quantity that will be used for further analysis.

Each individual TDC channel features a coarse time counter with a granularity of

5 ns and a fine time measurement block.

A delay line with individual delay elements and uniform delay along the path is setup for the fine time measurement. The number of crossed delay elements by a signal along the delay path defines a time value. This approach to time measurement is commonly referred to as the Tapped Delay Line (TDL) method.

Hereby a start signal initiates the propagation of the signal along the delay path. With the stop signal, which in this case is the next incoming rising edge, the output of the delay elements is latched. Being used as a start signal the system clock cycle limits the maximum fine time measurable cycle, which also defines the minimum length of the delay line as the maximum possible propagation time has to be longer than one clock cycle.

To optimise the resolution of the TDC the output data has to be calibrated as the temperature and fluctuations of the power supply may cause the delay time to vary. For this an artificial trigger is used creating randomly distributed hits in each channel over one fine time measurement interval. Afterwards the mean of all the delay times is extracted defining a delay time for each channel. With this assumption any deviation of the time signal between the channel has to originate from differences in the propagation delay. Thus the calibration pulls the ToT of each channel to the same predefined value. The corresponding calibration values are stored to be used in further analysis. Once a calibration has been executed it is valid for a given temperature and supply voltages. [10]

2.3.1 Results for time accuracy

The time difference between two DiRICH channels with the same input signal defines the timing precision. To test this a pulse generator emulating a pulse produced by a photomultiplier was used. In figure 2.6 this is depicted for different pulse voltages, the DiRICH shows excellent timing precision even with the lowest tested pulse amplitude of 1 mV with 61 ps RMS [13]. In comparison with the signal time difference of two of the used SiPMs, which is about 200 ps at FWHM [14], one can establish that the SiPM plus further possible signal spread in our setup, will be the limiting factor regarding precision not the DiRICH readout itself.

2.4 Trigger and Dataflow

A centralized system is necessary for the readout and synchronized triggering of all the DiRICH frontends. Here the CTS (Central Trigger System) and TRBNet work together to achieve this.

TRBNet: The TRBNet is a network protocol specially designed for data acquisition systems like the DiRICH. It is housed by the central FPGAs of the frontends and handles the communication amongst them and the CTS which is explained in
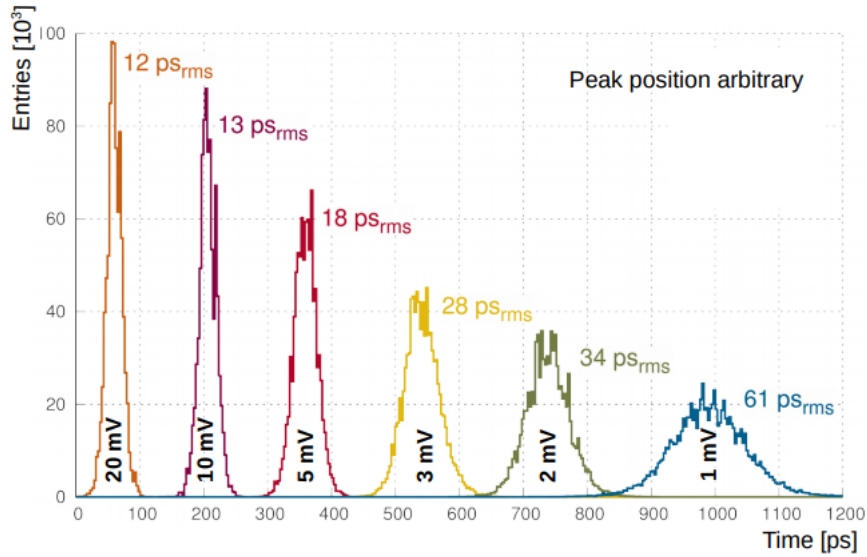
Figure 2.6: Graph of the timing precision of the DiRICH at different pulse amplitudes, measured with a pulse generator [13].

more detail later. The tasks of the TRBNet include a low-latency transmission of the trigger signals to all frontends, the subsequent data acquisition and slow control with which e.g. triggers can be switched on and off or the activity of the individual channels can be monitored.

The TRBNet runs on a network simply containing the CTS, frontends and hubs. The latter correspond to the part of the Data Concentrator which coordinates the communication and the forwarding of data to the event builder PC which itself is the hub of the network. [15]

When a trigger signal is received by the TDC the timing data is extracted during the in the trigger specified time window. In order to initiate and adjust the thresholds for a measurement corresponding scripts have to be executed on the event builder PC communicating with the DiRICH's TDCs via slow control. The threshold is given in natural numbers, with the conversion of $1 = 50.35\,\mathrm{mV}$. So for example when referring to threshold 1000 the threshold has a value of $1000 \cdot 50.35\,\mathrm{mV}$. The adjustability range of the possible threshold is $3.3\,\mathrm{V}$.

CTS: For any data acquisition system the trigger is a key part as it controls when constantly recorded data should be extracted and stored for further analysis. In this case the CTS which runs on the central FPGA of the Data Concentrator decides over the generation and forwarding of the triggers. In general it receives a trigger

source from a detector identifying physically relevant events and generates triggers accordingly. Additionally the CTS features an expandable modular structure, enabling the use of external trigger sources and an expansion via external trigger logic. A distinction is made between three different trigger sources: input signals from connected detectors, external triggers which expand the CTS's trigger logic potentially using it as a slave, and artificially generated triggers, e.g. by a pulser. By exploiting this modular structure any wanted behaviour of the CTS can be implemented. Commonly triggers are periodically forced regardless of the events occurring in the detector by using pulsers. Internally, this is supported by trigger logic which comprises 16 internal trigger channels (ITCs) to which various modules acting as trigger criteria e.g. aforementioned pulsers itself can be allocated. [15]

The CTS features a graphical user interface using the TRBNet's slow control to enable adjusting various parameters employed by the CTS by the user. For instance the ITCs can be separately configured to recognise rising edges or high levels and be switched on or off. Furthermore, the trigger type and the use of optional modules such as the pulsers can be set. Trigger type defines weather data from a detector output is taken or from an internal process e.g. for calibration purposes. Apart from the CTS the GUI also features TDC hit register monitoring providing real time feedback of the activity in each channel. [15]

The aforementioned detector event must not be confused with a CTS event in the eventbuilder. Naturally the CTS processes the data from the TDC and external or artificial trigger sources to produce a timing signal for the trigger. However during the trigger window, which corresponds to one CTS event, multiple or none actual physical detector events might occur. As an example one can connect a periodical pulser to an ITC causing regular trigger regardless of the actual events occurring leading to possible empty CTS events or with data for multiple detector events.

Since the forwarding of trigger signals and the data acquisition have entirely different requirements, the TRBNet carries out these tasks on separate paths to ensure low-latency transmission of the trigger signals for high trigger rate facilitating their synchronicity.

The TRBNet routes the trigger signals via a separate high priority channel from the CTS to all the frontends. As soon as all channels on the frontends have processed the trigger the next trigger can be accepted. Such a cycle only takes a few microseconds and is therefore possible trigger rates of several 100 kHz. When a trigger signal arrives, the data acquisition is initiated and the corresponding data is extracted and initially stored in the local frontend buffer. As soon as the CTS, which is always informed over the progress of the reading process, transmits the required signal the data is forwarded to a hub via a broadband connection where it can be stored to disk.

Chapter 3

RadMap Telescope

3.1 Objective

The Radmap telescope is a multi functional small form factor detector developed for the international space station. Dosimeters are used to measure the radiation dosage omnidirectionally. Additionally, the particle type can be identified and its track and direction determined using a cube of 4 individual fiber detectors. These fiber detectors, which from now on also referred to as *modules* feature 256 scintillating fibers each connected to a SiPM [2]. In total 12 modules were produced. With 8 of these two RadMap telescopes will be built. One of them will go to the ISS and a spare detector remains on the ground. For this project two modules from the remaining 4 spares will be used.

3.2 Scintillating plastic fiber detector

A scintillator in general emits photons when excited by radiation. By optically coupling a photomultiplier to a scintillator one can build a particle detector outputting an electrical signal when struck by radiation. Many scintillating materials are available, however, one suitable for such a detector naturally should be transparent to its own fluorescent light to allow transmission. Furthermore it should exhibit a highly efficient and linear conversion rate of absorbed energy to emitted fluorescent light, which allows a reliable absorbed energy to light output conversion. Additionally, a short decay constant enabling high timing precision and minimising detector dead time is desired.
In general the distinction between organic and inorganic scintillators is made, while subcategories do exist. Inorganic scintillators posses a greater stopping power, increasing absorbed energy and higher light output than organic scintillates but are quite brittle, rigid and often hygroscopic making them hard to handle. Furthermore, their response time is about 2-3 orders of magnitude slower [3].
For this detector the wide spread plastic scintillator, typically polystyrene mixed with an organic scintillator, was used. The plastic offers high flexibility and durability enabling a straight forward production process into the desired fiber shape.
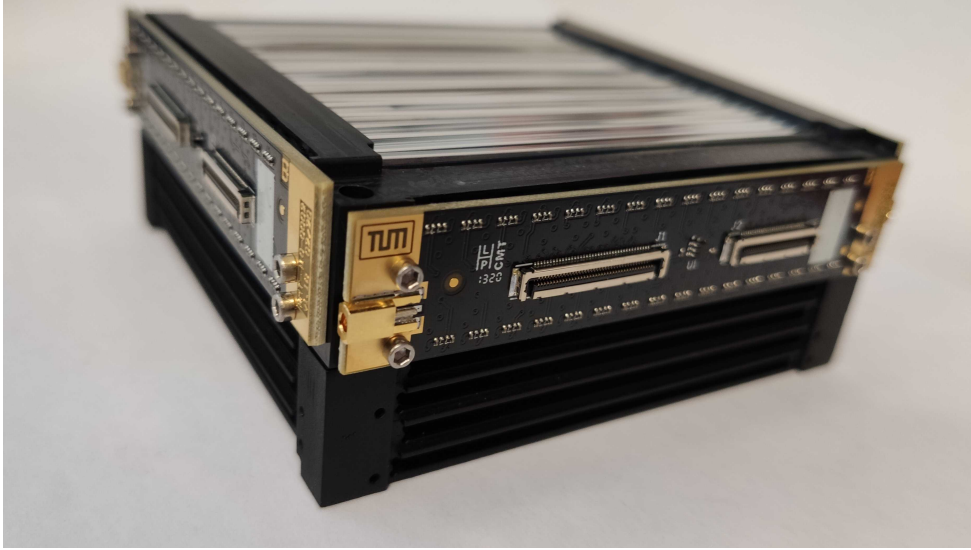
Figure 3.1: A fiber detector module standing on top of a mounting base. On the sides are the adapter boards, taking the output signal from the SiPMs and routing it the visible connectors. On the top one layer of fibers is visible.

The fibers were additionally clad with PMMA [16] aiming to protect the plastic from adsorbing foreign material and from abrasion as they will be exposed to the air. Furthermore, the fibers are coated with a thin aluminum layer to keep most ambient light from entering the detector. In total the fibers have 2 mm by 2 mm cross section and a length of 80 mm. The light travels through the fiber to the SiPM via total reflection, with a trapping efficiency of 4.2 %.

Each scintillating fiber is optically coupled to an individual SiPM, detecting the scintillation light and converting it into an electrical signal and further amplifying it.

Inside the modules the fibers are arranged in 8 layers with 32 fibers each. The orientation of the layers is alternating and every other layer has an offset of half a fiber's width orthogonal to its orientation. This way the entire detector surface area is covered in fibers.

The particle detection efficiency for MIPs was previously determined using pion beam data. In 2020 MIP pions with a momentum of $450 \frac{\text{MeV}}{c}$ were measured at the Paul Scherrer Institute in Switzerland with the Padiwa readout. The results showed a particle detection efficiency for each layer at roughly 90 %. This is explained by a dead region of the detector between fibers. Particles passing through the cladding or coating of the fibers, which is non scintillating, or small air gaps inbetween the fiber can not be detected.
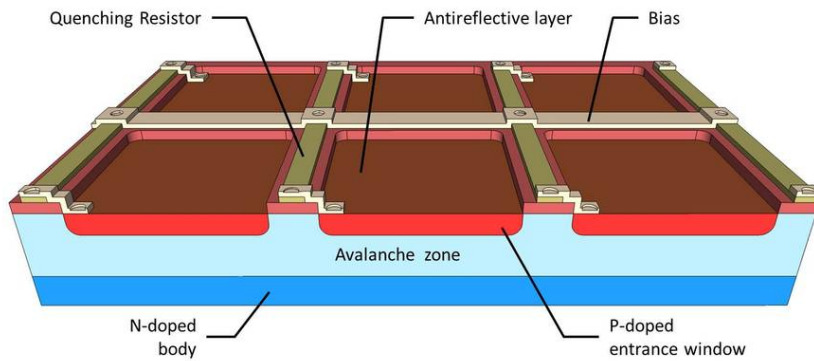
Figure 3.2: Schematic of a SiPM's micro avalanche photodiodes [14]

3.3 Silicon Photomultipliers

SiPMs combine the high light sensitivity of Photomultiplier tubes with the benefits of a solid-state detector which are mechanical robustness, low operational voltage and excellent response uniformity.

Silicon is a semiconductor effectively absorbing a wide range of wavelengths, especially in the visible spectrum, thus making it a suitable material for an avalanche photodiode. This will be further examined in the following.

A semiconductor can be doped with foreign atoms. This in general increases the conductivity of the material while also defining the dominant charge carriers. Dop-
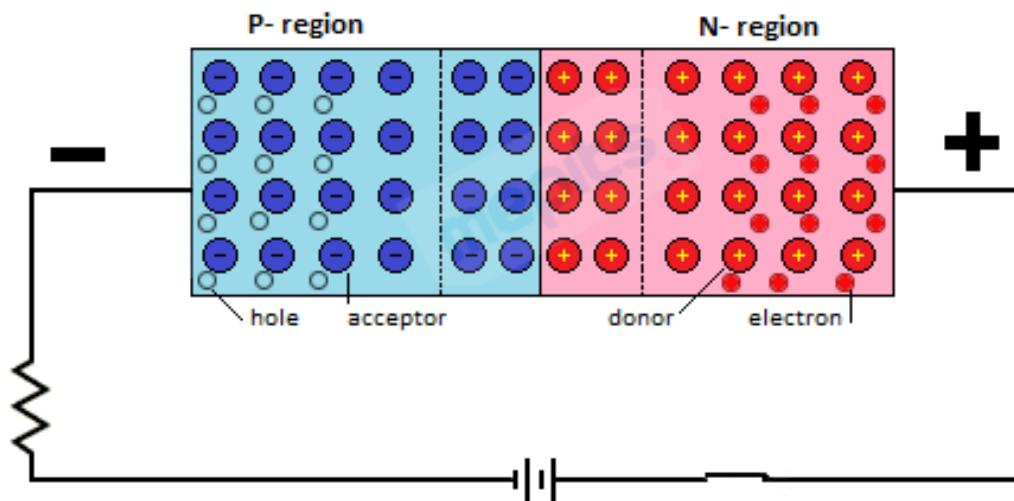
Figure 3.3: Schematic of pn-junction [17]

ing with electron donors increases the electron density resulting in a n-type, doping with electron acceptors increases hole density resulting in a p-type semiconductor. When bringing a p- and n-type semiconductor into contact a depletion zone with highly reduced charge carrier density and therefore exposed carrier material ions, a pn-junction is formed. Over such pn-junction current can flow with little resistance in one direction, but feels a high resistance and is virtually blocked in the other [18]. Figure 3.3 shows a schematic of a pn-junction.

Internally the SiPM is divided into multiple thousand square shaped micro avalanche photodiodes arranged in a grid spreading over the entire SiPM surface. Each of these pixels is formed by a pn- junction, over which a bias voltage and thus an electric field is applied (see figure 3.2). When a single photon is absorbed in such a diode it will create an electron hole pair. The charge carriers will, for strong enough fields, be accelerated to a point where they will produce more electron hole pairs resulting in a self perpetuating avalanche causing the silicon to become conductive and break down. This results in a macroscopic and measurable current. After the breakdown occurs the current is stopped by a series of quenching resistors limiting current drawn by the diode. This process lowers the bias voltage over the diode until the voltage falls below the breakdown voltage of the micro cell, thus stopping the avalanche [19, 20].

Our specific SiPM used in this setup is the PM3325-WB-D0 from the company KETEK. It has roughly 14000 micro cells per SiPM and a photon detection efficiency of up to 50 %, depending on the wavelength and overvoltage applied [21].

Chapter 4

Hardware and software developments for the detector setup

4.1 Adapter boards and signal chain

With the previously used Padiwa readout only half of the module could be read out simultaneously. However in order to perform effective particle tracking through the detector the whole module needs to be read out. This is made possible by the DiRICH as it has enough channels to read out all 256 channels of the module. To connect the module to the DiRICH a new signal chain featuring tow separate adapter boards was designed.

The first board (see figure 4.1a) is receiving the signal output for 64 channels from one of the module's adjacent boards (see figure 3.1) over two shielded cables, one carrying 30 the other 34 channels. The shielding of the cables is necessary so that the signal is not distorted during transmission. The board routs all 64 channels to a 80 pin connector which additionally transmits power. The power is provided directly by the DiRICH power board and can be used to power the modules. For this the board features a power connector. Furthermore, the board features a signal shaping filter for each channel. The output signal of a SiPM has a sawtooth shape with a steep leading edge followed by a long exponential decline (see figure 4.2), while the shaped signal is altered to feature a smooth peak (see figure 4.3). As the rising and especially falling edge is far clearer it improves the timing measurement of the TDC. Another reason to use such filters is to smooth out noise picked up by the signal.
The second adapter board (see figure 4.1b) features the same 80 pin connector as the first board. Over the corresponding cable it receives signal and power, and conducts both to pins which plug directly into the DiRICH backplane. There is also the option to mount the aforementioned filters on these boards.

Using the in the above described cables and adapter boards the signal is lead to the DiRICH. In figure 5.7 the assembled setup using one module is shown.
The signal chain had to be split up over two separate boards in the first place, because the cables connecting directly to the module are too short to directly plug into a adapter board for the DiRICH backplane. To solve this the 80 channel cables

(a)

(b)
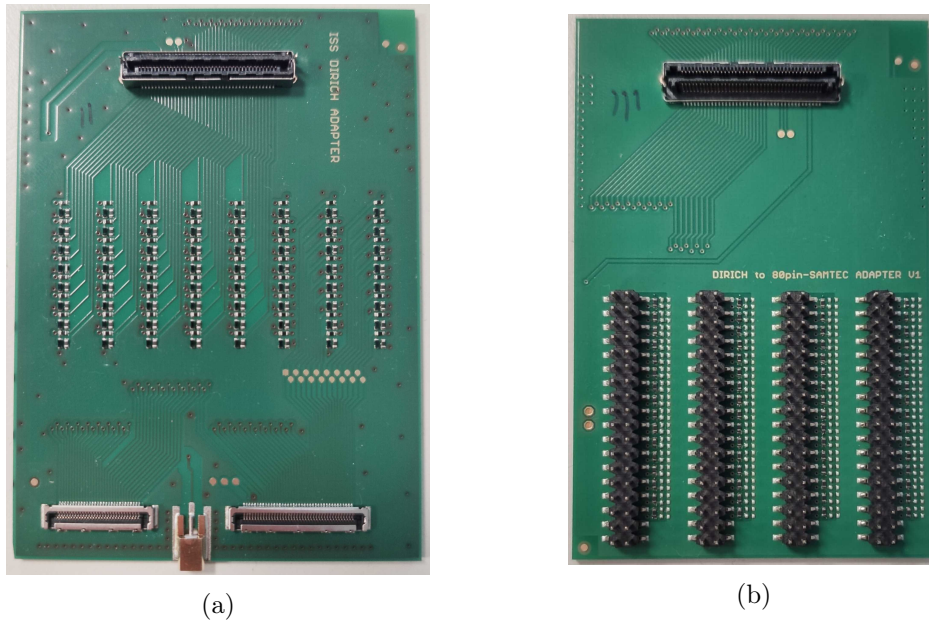
Figure 4.1:
(a) On the bottom, three connectors can be seen. The outer ones are the signal connectors and the middle one the power connector for the module. On the top is the 80 pin connector and inbetween are the filters.
(b) The bottom half shows the pins plugging into the backplane. On the top is 80 pin connector.
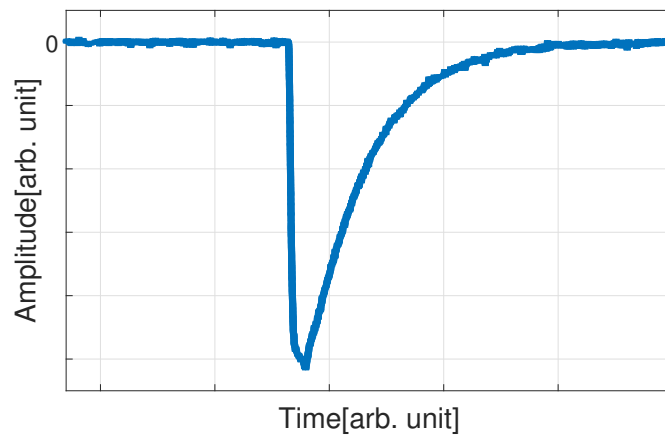
Figure 4.2: Raw SiPM output signal.
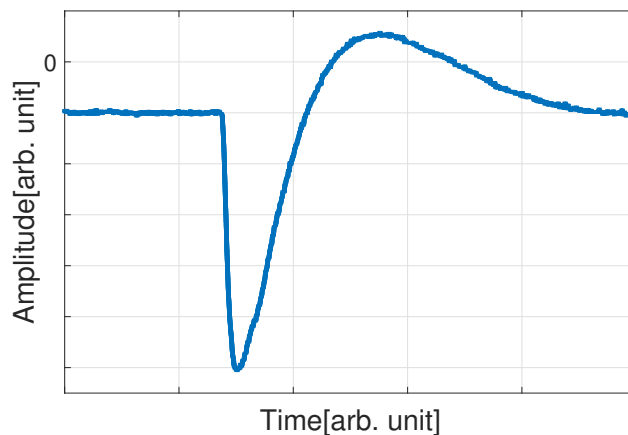
Figure 4.3: Shaped SiPM output signal.

were incorporated as an extension.

In total 6 boards can be plugged into the DiRICH backplane enabling the readout of 384 channels which corresponds to one and a half modules. However not all of the backplane slots can be served by the same adapter board, as the layout for the ground and power channels has two different orientations. Therefore, two sets of three boards with the respective channel layout were designed.

4.2 Mounting structure

In order to realise the experimental setup for the trigger and tracker system (see figure 1.2) a separate mounting structure had to be designed from scratch. Figure 4.4 shows the finished build. The fiber detector modules can be attached in the middle of the respective plates, on which the adapter boards will be mounted as well. In between the plates the photo-THGEM detector chamber which is standing on a table will be positioned.

Following requirements were set to the structure and subsequently realised during the design phase: the plates had to be height adjustable, to simplify the mounting of all components before setting the desired height. Additionally particle tracking is enabled for different distances between the modules. For this elongated holes were added to the poles enabling a smooth height adjustment. A friction grip from the backside of the poles using nuts fixes the plates in place firmly.

Furthermore, both plates had to be independently rotatable outwards to the side to

Figure 4.4: Pictures of the finished mounting structure from different angles.

facilitate any operations or adjustments on the detector chamber without having to disassemble the setup or move the mounting structure. This was implemented by splitting the pole into three separate parts and adding a second inside radius milled on the bottom, or jutting out the top of the poles when needed, enabling a smooth rotation of the individual poles and therefore the plates against each other. Using screws on the side of the poles the plates can be fixed in forward direction.

To guarantee the stability of both the plates mounted the the backbone and of the structure in general triangle shaped supports have been added at the respective places.

On the base plate 4 threads were added aiming to balance the the structure, by adjusting the corresponding screws protrusion on the down side of the base counteracting any unevenness of the ground.

All parts were designed in the CAD software SOLIDWORKS and manufactured by the Zentralwerkstatt at the TUM physics department.

4.3 Adjusting software from Padiwa readout

For the previously used Padiwa readout of the module an analysis framework was already available. This was used as a basis for the DiRICH analysis and adjusted or

expanded upon when necessary.

As a basis for any further analysis the mapping from fiber position inside the module to the channel and TDC numbers was implemented first. The DiRICH supports the readout one and a half modules. Different mapping configurations were added to cover different scenarios, for instance the read out of one full module and every second layer on the other. With the mapping as a basis all further analysis such as particle tracking can be implemented.

But first the ToT values for each event have to be determined from acquired data, which is stored in raw data files. The data is stored event by event as given by the CTS and holds the event number and the time stamps of all rising and falling edges for each event. Since we wanted to use the ROOT framework [22] for the analysis the raw data files were converted to the .root format with the help of the GO4 framework [23] which brings the desired functionality. Still, however, the ToT values have not yet been determined from the rising and falling edge data. For this and to map the channel and TDC numbers to actual fibers within the module a ROOT macro is used which was expanded and adjusted for this project. All further analysis such as time calibration (see section 5.2) and the corresponding macros were based on ROOT.

Chapter 5

Measurements and Results

5.1 Testing setup for calibrations

For various tests and measurements, especially for calibration, a signal source generating a consistent signal at high rates is desired. So that sufficient statistics can be collected in a reasonable time frame. To achieve this a single SiPM, the same model which is used in the module, was illuminated with a LED emitting periodic flashes of light at a frequency of 100 Hz. The light intensity of this flasher could be adjusted via a USB connection to a computer. In order to keep any ambient light from hitting the SiPM the setup was housed in a dark box.

5.2 Time calibration

In order to enable particle tracking a time calibration had to be implemented as the arrival time of the signal as measured by the TDC varies between different channels. The main reason for this time difference is that inside the FPGA each channel has its individual path while the path lengths can wildly vary. Other differences in the signal chain between the channels such as differing lengths or angles on the adapter boards or in the DiRICH backplane are not expected to make a significant difference.The measurements for the time calibration were taken using the flasher and a single SiPM as discussed before. Here the output signal was split evenly between two adapter boards, 16 channels each, which plug directly into the DiRICH backplane. One of the boards stayed plugged in on the same position through the entire measurement to provide reference. The other board was moved through all the other slots on the backplane each time staying plugged in for a few minutes.

Each TDC has its own reference time stored in channel 0. The reason for this is that the absolute time varies between TDCs. So in order to compare time stamps between TDCs the respective reference time needs to be subtracted from the time stamps first. To implement the time calibration a reference channel was picked to which all other channels are compared. Channel 2 on TDC 1200 was chosen arbitrarily as the reference channel. For every signal in a channel its arrival time
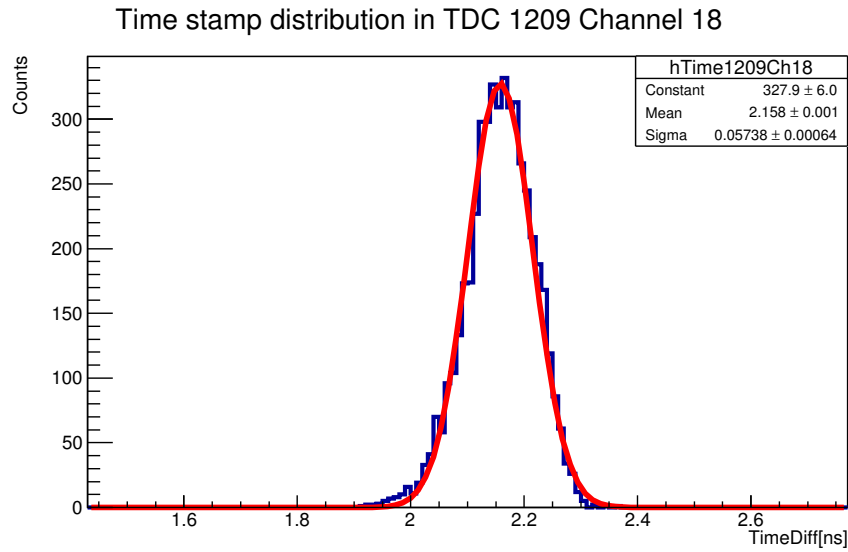
Figure 5.1: 1-D histogram of the time difference in ns with Gaussian fit in one channel.

and the time stamp is stored together with the channel 0 reference time. First this reference time be subtracted from the time stamp to make the TDCs comparable as mentioned before. Now for every signal the difference between the channel 0 corrected time stamp and the arbitrarily chosen reference channel is filled into a histogram for each channel individually. The resulting distribution of the time difference for one exemplary channel is shown in 5.1 together with a Gaussian fit. Aiming to apply the time calibration in further analysis the mean of the fit was used to set the value of the time difference for each channel individually.

Figure 5.2 shows the time difference distribution for channels in one TDC before calibration. After applying the determined time correction the signals in different channels arrive at the same time as expected. This can be seen in figure 5.3.

Figure 5.2: Exemplary 2-D histogram of the **uncalibrated** time difference in ns for each channel in one of the TDCs.

Figure 5.3: Exemplary 2-D histogram of the **calibrated** time difference in ns for each channel in one of the TDCs.

5.3 Determination of expected time over threshold for cosmic particles

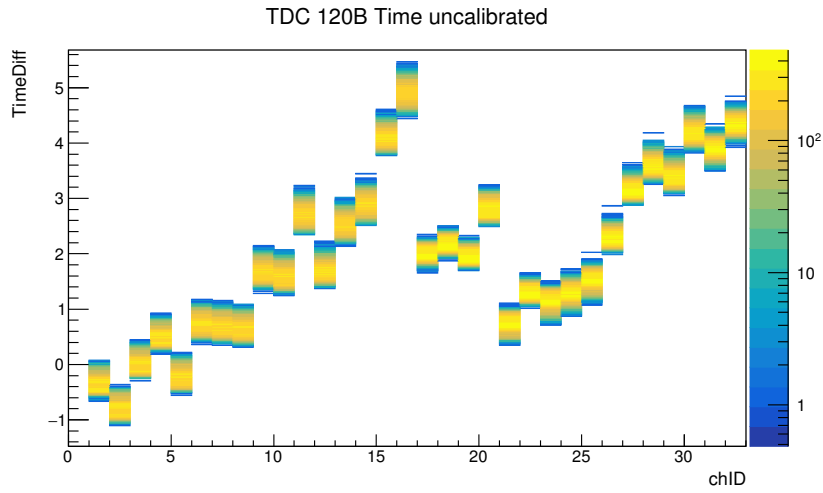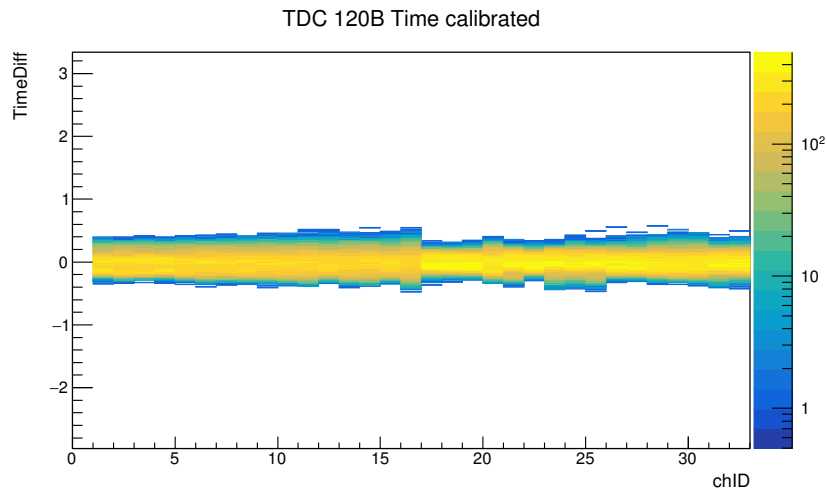Figure 5.4: ToT histogram, measured with LED flasher and single SiPM at a threshold of 100 plus Gaussian fit for Padiwa in pion MIP range.

In order to understand which ToT values are expected from measuring cosmic radiation with the DiRICH setup, pion MIP data which was recorded with Padiwa setup was used. The cosmic radiation is expected to be mainly muons in the MIP range. Therefore, one could emulate a signal with the LED flasher and the single SiPM that produced a very similar signal as the MIP pions in an arbitrarily chosen channel in the Padiwa setup and use the same signal as input for the DiRICH setup. With this technique one could measure a MIP-like signal with the DiRICH.

The ToT distribution from an exemplary run in the beam time in the chosen channel of the Padiwa can be seen in figure 5.6. The peak ToT value measured with the MIP pions is 15.3 ns and was obtained by taking the mean of a Gaussian fit curve for the ToT distribution.

The histogram for the MIP-like signal in the padiwa is shown in figure 5.4 with a mean ToT of 15.1 ns. The minimum adjustment step for the flasher, however, didn't allow for the ToT to be more closely adjusted to the pion peak ToT. Continuing, the according ToT distribution for the DiRICH is shown in figure 5.5 with a mean of 15.5 ns.

With this a rough estimate for the expected cosmic muon MIP ToT measured by the DiRICH was made: The difference of the pion MIP ToT and the imitation
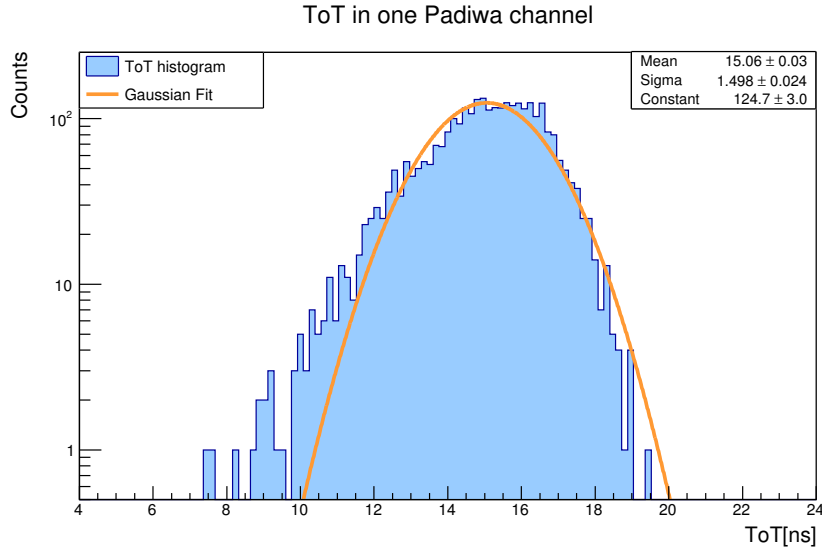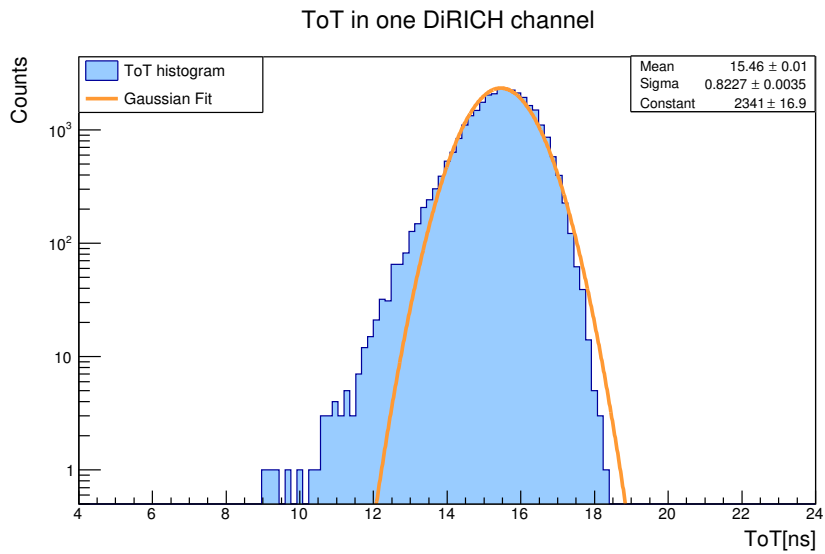
Figure 5.5: ToT histogram, measured with LED flasher and single SiPM at a threshold of 100 plus Gaussian fit for DiRICH in pion MIP range.
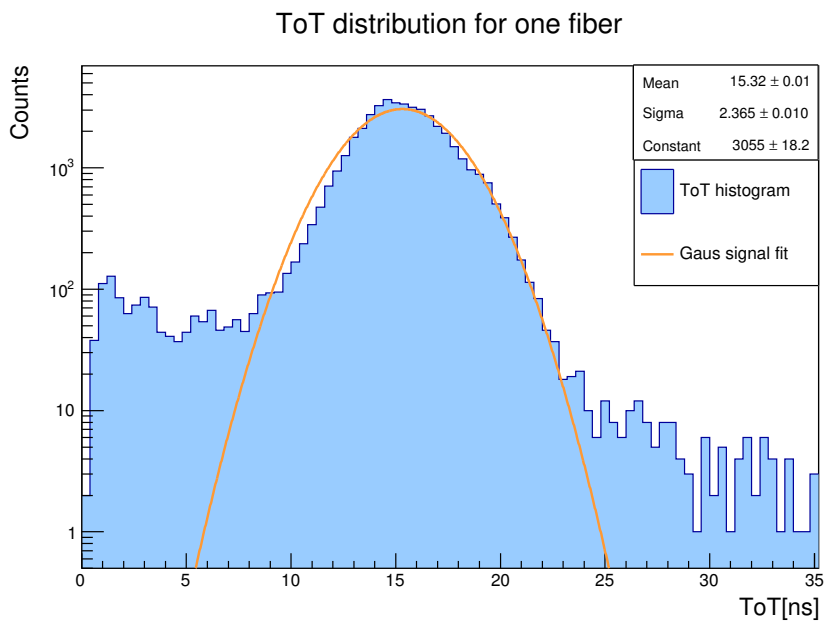

Figure 5.6: Pion MIP ToT histogram with Gaussian fit.

29
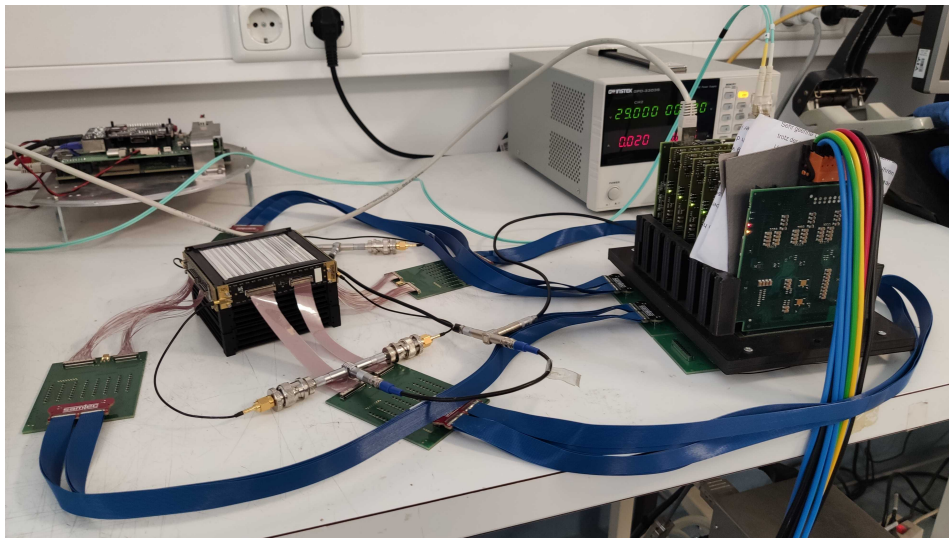
Figure 5.7: Test setup for cosmic ray measurement without light proof cover. On the right is the DiRICH with adapter boards plugged into its backplane. They are connected via the blue cables to the next set of adapter boards connected which are in turn connected over two cables to the module. Behind the DiRICH is the power supply powering all four sides of the module with a single output channel.

measurement, which is $15.3 - 15.1\,\text{ns} = 0.2\,\text{ns}$ was added to the mean ToT measured by the DiRICH giving the expected ToT for MIPs of $15.7\,\text{ns}$. For a rough estimation this is justified as over such a small interval the energy loss is linear to the ToT. Notably when comparing the $\sigma/mean$ for both measurements the Padiwa's $\sigma_{Padiwa}/mean_{Padiwa} = 0.10$ is almost double than the DiRICH's $\sigma_{DiRICH}/mean_{DiRICH} = 0.053$ meaning that the energy resolution of the DiRICH is about twice as good.

5.4 Cosmic ray measurements results and analysis

5.4.1 Cosmic ray measurement setup

The setup used for cosmic particle measurements is shown in figure 5.7, with which all SiPMs of the module were read out. From each side the signal was transmitted to the DiRICH via the signal chain described in section 4.1. Note that for the measurement the module was covered so that no ambient light can reach the detector and distort the measurement.

Multiple cosmic ray measurements, mostly running overnight or over the weekend have been done with the threshold varying between 100 and 1300. In the following sections the data will be analysed and interpreted while being inspected and high-
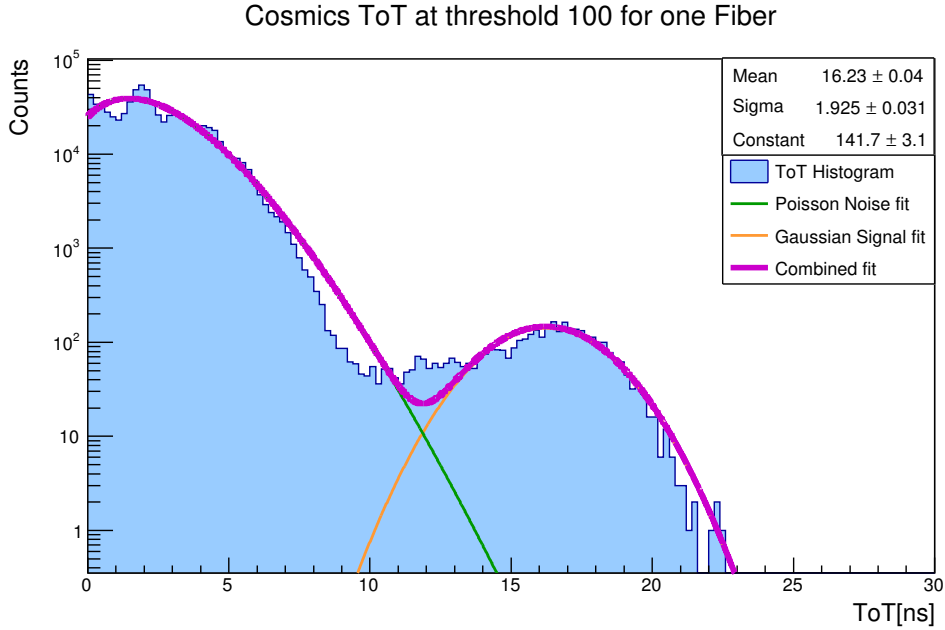
Figure 5.8: ToT distribution of a cosmic ray measurement at a threshold of 100. The noise fit represents a Poission distribution and the signal is fitted with a Gaussian function. Additionally, a fit with the sum of both functions, the combined fit, is drawn. The statistics box on the top right shows the fit parameters of the Gaussian fit.

lighted from different perspectives.

5.4.2 ToT distribution of cosmic particles

Figure 5.8 shows a ToT histogram of an overnight cosmic ray measurement at a threshold of 100 for the same channel as used for the comparison with the Padiwa in the previous section. The noise was fitted with a continuous Poisson distribution while the combined signal from cosmic rays and background radiation was fitted with a Gaussian distribution. Additionally, the sum of Poisson and Gaussian distributions was used to fit signal and noise together. The Gaussian fit has a mean of 16.2 ns and a $\sigma/mean$ ratio of 0.12. As described in the previous section MIPs would be expected at around 15.7 ns ToT but with a slightly higher $\sigma/mean$ than the $\sigma_{DiRICH}/mean_{DiRICH} = 0.053$ from before as the scintillator itself naturally introduces some signal spread due to statistical variations in energy loss and photon trapping.

Cosmics ToT at threshold 1300 for one Fiber
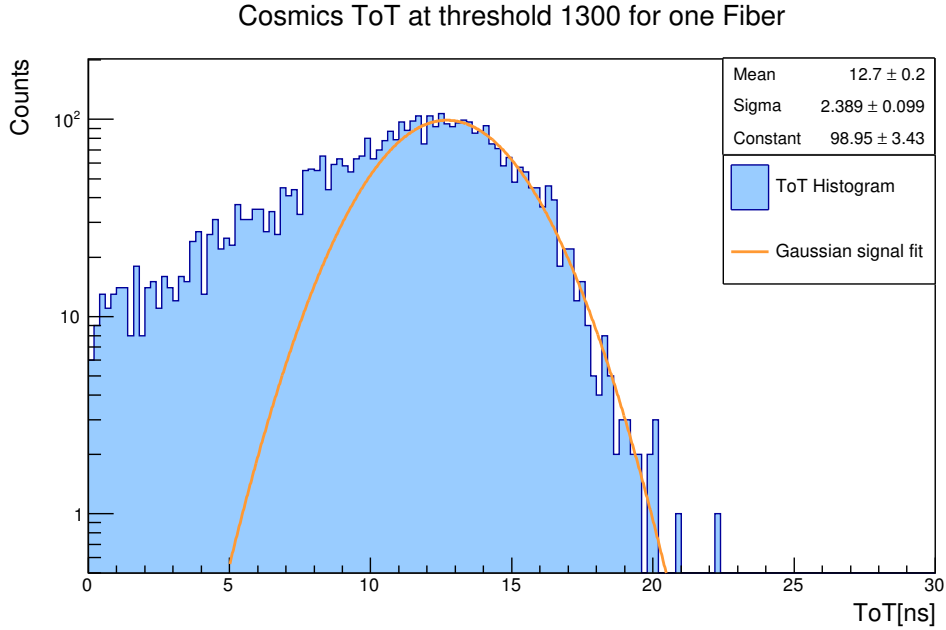

Figure 5.9: ToT distribution of a cosmic particle measurement at a threshold of 1300. The signal fit function is Gaussian. The statistics box on the top right shows the fit parameters of the Gaussian fit.

In addition to cosmic muons MIPs also background β-particles are expected, which show similar energy loss (see section A.1) and thus result in similar ToT values.

Considering the $\sigma/mean$ here is more than double of what would be expected for purely MIPs, the energy loss of the particles within a fiber must vary. This can be explained when taking into consideration that, for a cosmic ray measurement not all measured particles cross a fiber vertically but particles coming in at an angle might cross a fiber diagonally resulting in a higher ToT, or only parts of a fiber resulting a lower ToT. This is illustrated in figure 5.10. Keeping in mind the larger $\sigma/mean$ the peak of the ToT distribution at a higher ToT is within expected deviations.

At the lower end of the spectrum the signal overlaps with the noise and no clear distinction can be made. The fit functions help to separate signal from noise and the combined fit function describe the measurement rather well. When comparing this to a cosmic measurement recorded with a higher threshold, as depicted in figure 5.9, where the majority of electronic noise is below the threshold, still a tail can be observed at lower ToT values far below MIP range. One reason for this is, particles passing only through small parts of the fiber as described above. Another reason could be low energy background electrons, i.e. with an energy lower than the energy loss for MIPs in one fiber getting absorbed within the fiber. In order to account for
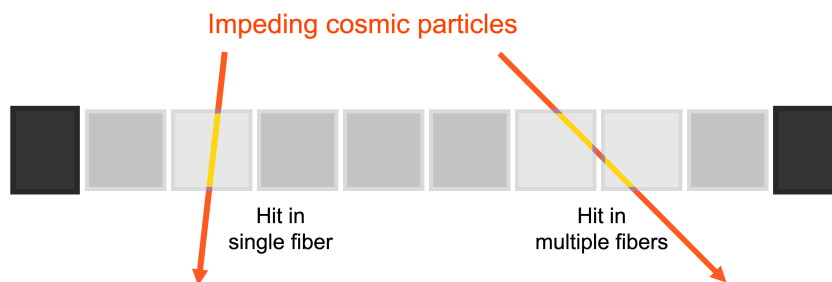
Figure 5.10: Particles passing through fiber cross section in different angles. Graphic by Berkin Ulukutlu.

this possibility one would need to model the signal with a different function better resembling the shape seen for high threshold measurement. The Gaussian fit is still justified as it models the peak of the ToT distribution very well, giving a reliable way to determine the signals mean ToT.

Figure 5.11 shows a plot of the mean ToT as a function of threshold. The measurements that were used to determine these mean and σ values, which were not shown before can be found in the appendix A.2. As one would expect, as the threshold increases it moves closer to the SiPMs output signal peak and the ToT decreases. The plot shows a straight line fit to demonstrate this.

5.4.3 Coincidence

When signal is measured in two different places in one detector or in two entirely separate detectors at the **same time** we speak of a coincidence. In this case the cosmic coincidence is examined between two different layers of the fiber detector. Therefore, first one needs to define within what time interval two signals a considered "at the same time". Here for testing purposes the coincidence time of 5 ns has been chosen considering the low cosmic rate this should be sufficient. Apart from testing, this time interval should be set as small as possible to provide the most accurate results. The minimum interval is given by the time resolution of the detector.

Figure 5.12 shows a coincidence plot for the top layer (L1) and bottom layer (L8). The plot was created by checking which pairs of two hits occurred at the same time in layer 1 and 8 and filling their corresponding ToT values into the histogram. The peak at roughly 16 ns ToT for both layers represents cosmic particles. The probability that this peak contains background radiation is very low because, as discussed before most β-particles will be scattered out of the module or absorbed
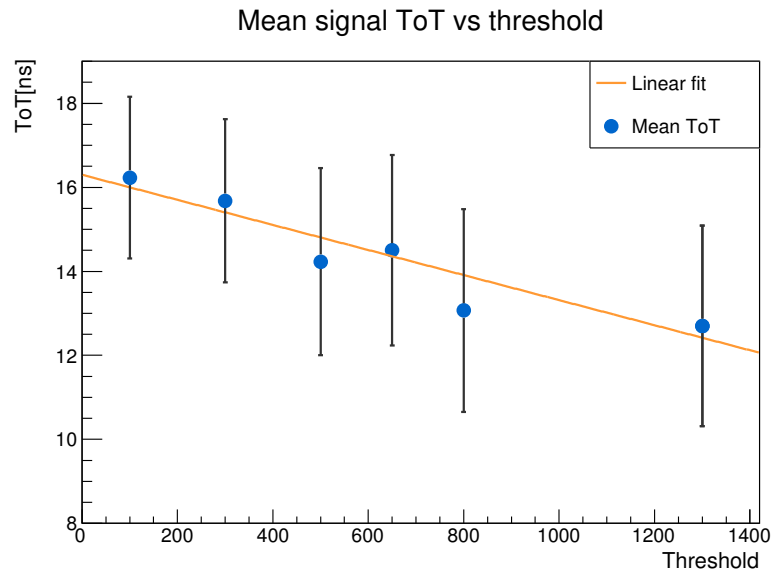
Figure 5.11: Mean ToT retrieved from Gaussian fit plotted as a function of threshold. The error bars represent the σ of the Gaussian.
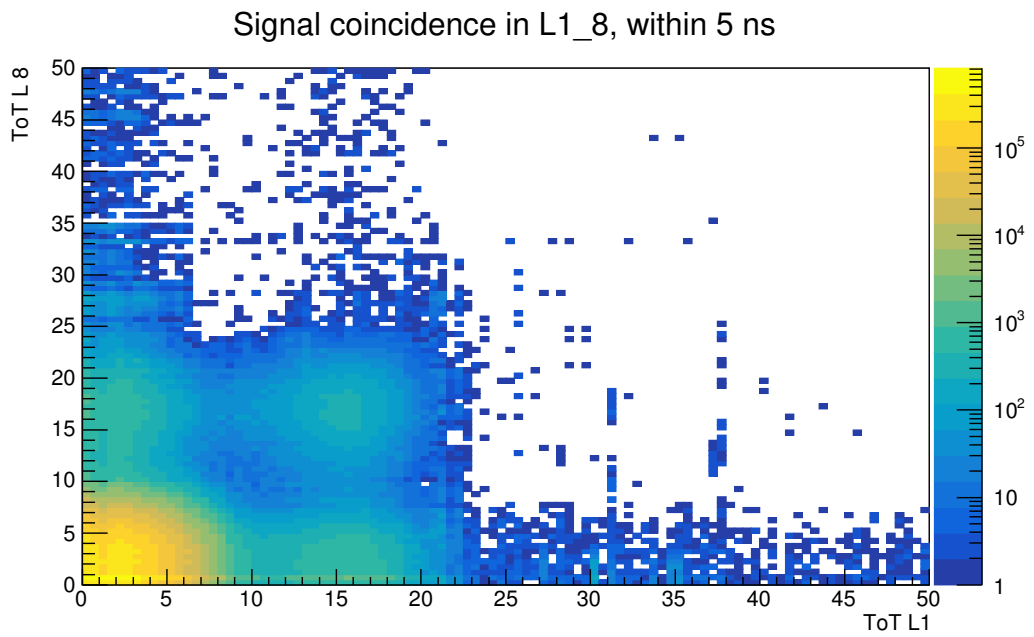

Figure 5.12: Coincidence between Layer 1 and 8 within 5 ns at a threshold of 300.

entirely within a few layers. To further decrease this probability not only the signal time but also the position needs to be restricted. But only with proper tracking it is possible to distinguish single cosmic particles from background particles. At the bottom and left edges of the plot where the recorded hits have ToT close to 0 ns, coincidence between cosmic particles at roughly 16 ns and noise can be seen. Furthermore, the area in the left corner where both axes are close to 0 ns shows noise coincidence. This is expected for random noise.

5.4.4 Clustering

The next step towards particle tracking was to group signals originating from a particle passing through the detector into so called clusters. Since particles traversing the detector can, depending on the incoming angle, hit multiple fibers (see figure 5.10) within one layer one needs to make sure to associate the signals with the corresponding particle. For this reason clusters were created.
A cluster consists of at least one signal and holds position, time, and ToT information. The position and time is weighted with the ToT value of the corresponding signals. This way, the position resolution becomes better than just one fiber width. Also, a cluster contains only signals from within one layer. So when such clusters are used for particle tracking later, a track can only contain up to one cluster per layer crossed.
 The clustering process works as follows. For the first layer one looks for all signals within the ToT range where MIPs are expected. Then starting with the largest ToT signal a cluster is created and all signals from neighboring fibers are added to the cluster if they are within a certain time window, in this case 5 ns. Note that both this time interval and the number of the included fibers can be adjusted if this shows to be necessary. Signals that were added to a cluster are marked as "used" so that one makes sure that no signal is associated to multiple clusters. This step is repeated until no signals within the MIP ToT range are left. After the first layer is done the process is repeated for all layers. A possibility to get an idea about the qualitative angle distribution of the traversing particles before the actual tracking is done is to look at cluster positions between layers for clusters within the coincidence time window. Figure 5.13 shows such plots for different layers 1 and 3 , 1 and 5, 1 and 7, and 1 and 6. It would be expected to see cluster coincidence farther away from the diagonal with increasing distance between the layer as particles passing through the module at an angle will simply move partly sideways as they move down through the detector. This can be clearly seen here as the cluster coincidence smears out from the diagonal with increasing distance between the layers.
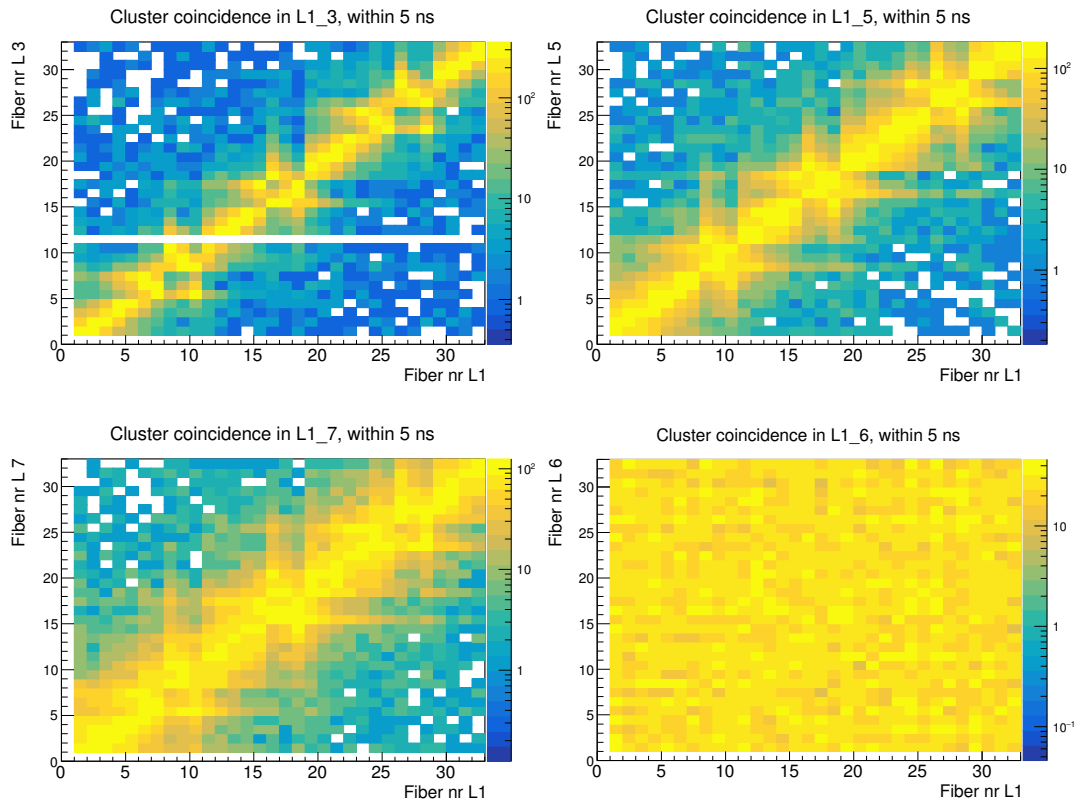
Figure 5.13: Cluster coincidence for different Layers. The x- and y-axis represent the fiber numbers for the respective layers.

This cluster coincidence can of course only be seen between layers that point in the same direction that is why before only the odd layers have been examined. The plot in the bottom right corner of figure 5.13 shows the cluster coincidence plots for two orthogonal layers just giving a random distribution as there is naturally no correlation between the x and y direction.

Chapter 6

Summary and Outlook

In the course of this thesis a new detector setup capable of tracking particles has been developed. It uses the scintillating fiber modules developed for the RadMap project as peripheral detectors for tracking. Inside the module, the fibers are arranged in orthogonal layers. This structure enables particle quasi-omnidirectional tracking of impeding particles. The DiRICH system is used as a readout for the modules, which receives the output signal from the SiPMs of the module and determines its ToT for an (adjustable) threshold.

To establish the interface between the module and the DiRICH two separate adapter boards have been designed. For the readout of the module, an analysis framework has already been developed for a different project using a Padiwa based readout. This has been modified and adjusted to work with the DiRICH system. With the detector setup assembled, long-duration cosmic tests and time calibration measurements were conducted. The cosmic measurements were analyzed in detail with one key assumption in mind: the measured cosmic particles are muons. This is justified as the vast majority of cosmic rays at sea level are muons. It was established that for conditions of this measurement the expected cosmic muons are in the MIP energy range. So, pion MIP data from a previous beam time was used to understand which ToT values are expected for cosmic particles. These estimations have been found to stand in very good agreement with the measured ToT distribution for cosmic particles.

Continuing the time calibrations measurement were conducted using a LED regularly flashing a single SiPM. The time calibration is needed as the signal arrival time measured by the TDCs varies between channels. To implement this the analysis software was further developed, and in subsequent tests it was observed that the time calibration is functioning properly.

With this, the signal coincidence between different layers of the module could be analyzed. A clear coincidence can be seen between signals in two distant layers of the module. This further confirms that the peak in the ToT distribution is caused by cosmic and not just background β radiation. β-particles exhibit a similar energy loss to cosmic muons but have far lower energy. Thus β-particles are likely to be scattered out of their straight path and therefore don't show coincidence.

First developments towards particle tracking have been made on the software side. Signals in one layer caused by the same particle are arranged into clusters. The clusters show a reasonable coincidence between layers already hinting towards proper tracks. Considering the tests and analysis this detector setup is deemed to be operating as intended.

An obvious next step would be to continue developing the tracking to take clusters from each layer and from that build a track first through one module and then two vertical modules In the broader view, it is foreseen to expand this particle tracker to also function as a trigger. For this, the DiRICH will be additionally used to generate and forward a trigger signal to the readout of a photo THGEM detector. The trigger should only be sent if a cosmic particle has been identified so that it is possible to distinguish wanted events from unwanted ones. For this setup of the trigger and tracker system, a mounting structure was already designed and manufactured.

Acknowledgements

First i want to thank Prof. Laura Fabbietti without whom this thesis would not have been possible. A special thanks goes to my advisor Thomas Klemenz who guided me through this project and always patiently explained things over and over and corrected my thesis without getting annoyed. I also want to thank Berkin Ulukultu for always helping me with the measurements and providing great graphics. Additionally i want to thank my girlfriend and family who always supported me.

Appendix A

Appendix
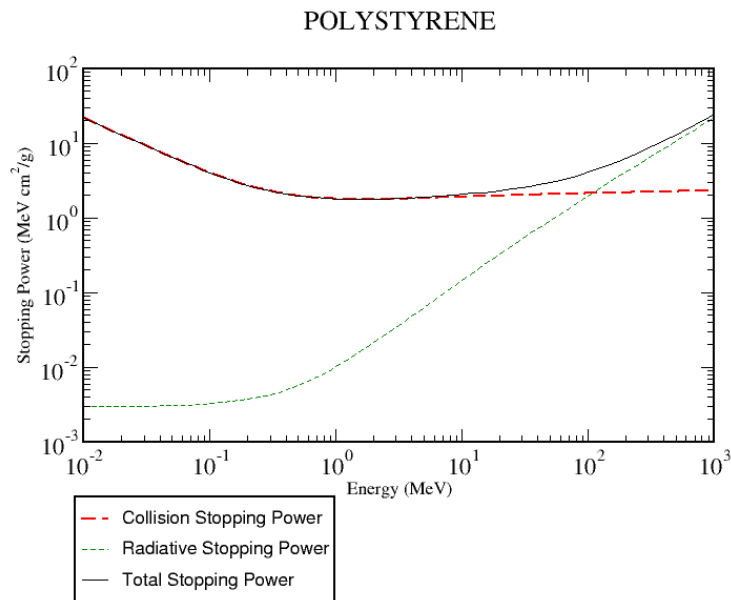
A.1 Electron energy loss

POLYSTYRENE

Figure A.1: Total, collision and radiation electron energy loss versus energy in polystyrene normalized to density [24].

Within the energy range of β-particles electrons largely show a energy loss of $-\frac{1}{\rho}\frac{dE}{dx} = 1.9\frac{\text{MeV}}{\text{g}^{-1}\text{cm}^2}$ (see figure A.1) in polystyrene which is the same as for cosmic MIPS [3]. At lower energies lower than 0,6 MeV the energy loss rises significantly.

Figure A.2: ToT histogram of cosmic ray measurement at a threshold of 300. The noise fit represents a poission ditribution and the signal fit Gaussian. Additionally a fit with the sum of both functions, the combined fit is drawn too. The statistics box on the top right shows the fit parameters of the Gaussian fit.

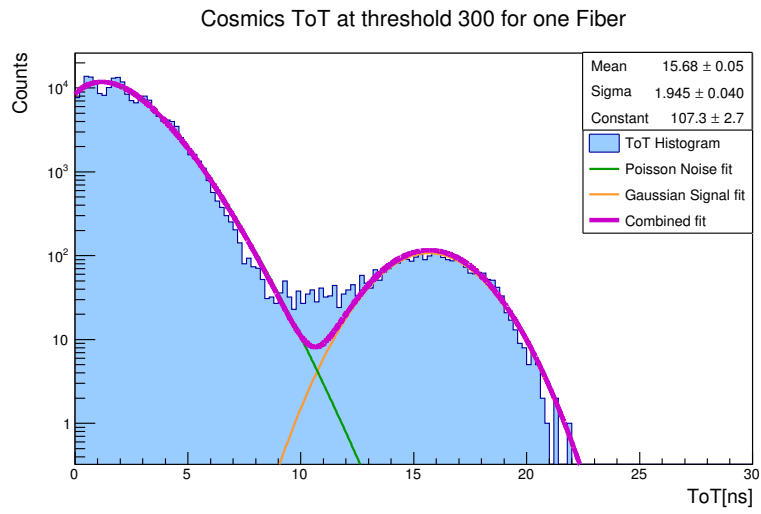## A.2 Additional ToT distribution plots

Figure A.3: ToT histogram of cosmic ray measurement at a threshold of 500. The noise fit represents a poission ditribution and the signal fit Gaussian. Additionally a fit with the sum of both functions, the combined fit is drawn too. The statistics box on the top right shows the fit parameters of the Gaussian fit.
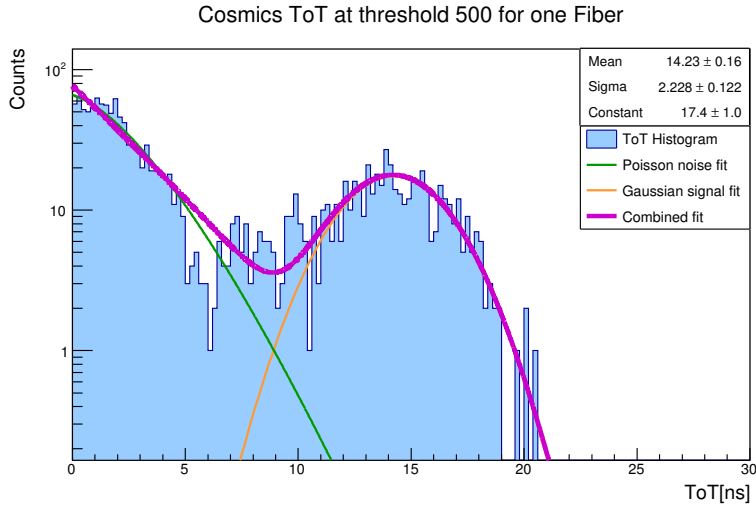

Figure A.4: ToT histogram of cosmic ray measurement at a threshold of 650. The noise fit represents a poission ditribution and the signal fit Gaussian. Additionally a fit with the sum of both functions, the combined fit is drawn too. The statistics box on the top right shows the fit parameters of the Gaussian fit.
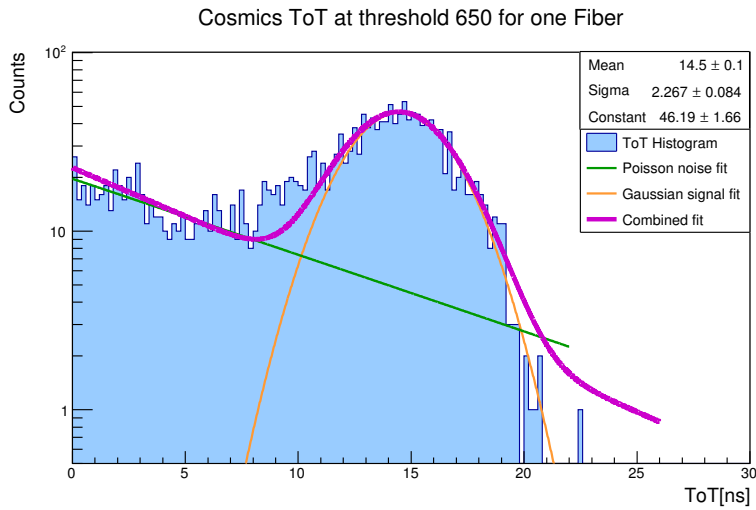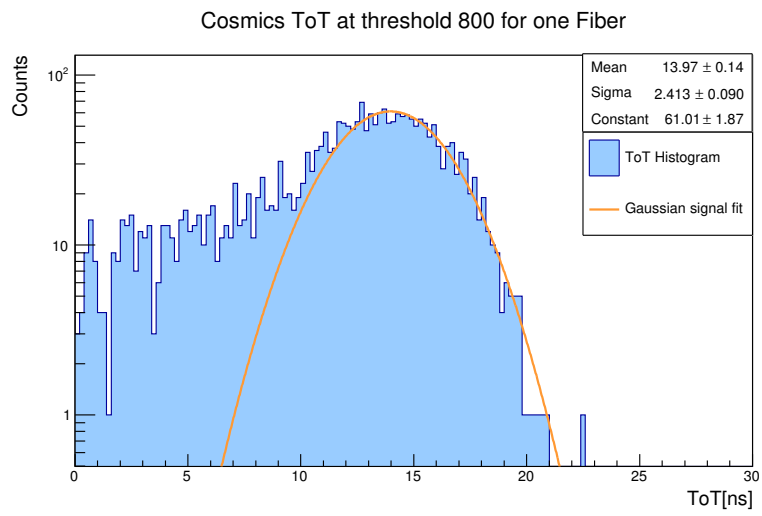
Figure A.5: ToT histogram of cosmic ray measurement at a threshold of 800. The signal fit function is Gaussian. The statistics box on the top right shows the fit parameters of the Gaussian fit.

Bibliography

[1] **J. Spanggaard, P. Carriere, S. Duarte Pinto, G. Tranquille** GEM Detectors for the Transverse Profile Measurement of Low Energy Antiprotons and High Energy Hadrons `https:// www.researchgate.ne t/publication/290229929_Gem_detectors_for_the_transverse_profile_mea surement_of_low_energy_antiprotons_and_high_energy_hadrons`

[2] **Martin J. Losekamm; Stephan Paul; Thomas Pöschl; Hans J. Zachrau** The RadMap Telescope on the International Space Station. `https:// / ieeexplore.ieee.org/ abstract/ document/ 9438435?casa_token= 5uv4KAq46F4AAAAA:s_PVKWtocuWVeYcRsx_WfL8g4gt_H4OibExIFKAJSokJAnLlDt NTTgTF8OGg_Tygjr6rLvILBxUw`

[3] **W. R. Leo** Techniques for Nuclear and Particle Physics Experiments, Second revised edition, Springer Verlag

[4] **Cern** Cosmic rays: particles from outer space, `https://home.cern/science /physics/cosmic-rays-particles-outer-space`

[5] **Vlado Valković,** Radioactivity in the Environment, Elsevier Science, 2000, `https://doi.org/10.1016/B978-044482954-2.50002-2`

[6] **PDG**: Cosmic Rays, Revised October 2019 by J.J. Beatty (Ohio State U.), J. Matthews (Louisiana State U.) and S.P. Wakely (Chicago U.; Chicago U., Kavli Inst.), `https://pdg.lbl.gov/2000/cosmicrayrpp.pdf`

[7] **Halil Arslan, Mehmet Bektasoglu** Angular and energy distribution for parent primaries of cosmic muons at the sea level using Geant4 `https://doi.org/10. 1016/j.nima.2015.01.010.`

[8] **Adam, W. and Bergauer et al.** Performance studies of the CMS Strip Tracker before installation. `https://www.researchgate.net/publication/47684440_ Performance_studies_of_the_CMS_Strip_Tracker_before_installation`

[9] **K.A. Olive et al.**(Particle Data Group), Chinese Physics C38, 090001 (2014). `https://doi.org/10.1088/1674-1137/38/9/090001`

[10] **Grzegorz Korcyl, Ludwig Maier, Jan Michel, Andreas Neiser, Marek Palka, Manuel Penschuck, Pawel Strzempek, Michael Traxler, Cahit Ugur**: A Users Guide to the TRB3 and FPGA-TDC Based Platforms `http://trb.gsi.de/`

[11] **GSI Helmholtzzentrum für Schwerionenforschung GmbH** TRB, `https://www.gsi.de/work/forschung/experimentelektronik/digitalelektronik/digitalelektronik/module/trigger_synchronisation/trb?no_cache=1`

[12] **Michael Traxler** TRB/Padiwa/ DiRICH FEE electronics with 10ps precision FPGA-TDCs for MA-PMT/MCP-PMT readout, URL: `https://indico.cern.ch/event/565957/contributions/2286375/attachments/1338642/2014952/8-MichaelTraxler_trb_applications.pdf`

[13] **C. Pauly** Status of the CBM- and HADES RICH projects at FAIR, URL: `https://www.researchgate.net/publication/331766089_Status_of_the_CBM_and_HADES_RICH_projects_at_FAIR`

[14] **David Schug, Vanessa Nadig, Bjoern Weissler, Pierre Gebhardt and Volkmar Schulz** Initial Measurements with the PETsys TOFPET2 ASIC Evaluation Kit and a Characterization of the ASIC TDC, URL: `https://www.researchgate.net/publication/329398251_Initial_Measurements_with_the_PETsys_TOFPET2_ASIC_Evaluation_Kit_and_a_Characterization_of_the_ASIC_TDC`

[15] **Manuel Penschuck** Development and Implementation of a Central Trigger System for TrbNet-based systems, URL: `http://hades.gsi.de/sites/default/files/web/media/documents/thesis/Bachelor/Development_and_Implementation_of_a_Central_Trigger_System_for_TrbNet-based_systems_M._Penschuk_2013-Aug.pdf`

[16] **Sabrina Kressierer** Construction of a Scintillator Fiber Detector for Space Applications.

[17] **Apogeeweb** How is PN Junction Formed? Basics and Examples, URL: `https://www.apogeeweb.net/electron/how-is-pn-junction-formed.html`

[18] **Siegfried Hunklinger** Festkörperphysik 3. Auflage, Oldenbourg Verlag München

[19] **SensL Technologies Ltd.** An Introduction to the Silicon Photomultiplier, URL: `https://www.sensl.com/downloads/ds/TN%20-%20Intro%20to%20SPM%20Tech.pdf`

[20] **AP Technologies Ltd** Introduction to SiPM Technology, URL: `https://www.aptechnologies.co.uk/support/SiPMs/intro`

[21] **KETEK GmbH** Product Data Sheet, URL: `https://www.ketek.net/wp-content/uploads/2018/12/KETEK-PM3325-WB-D0-Datasheet.pdf`

[22] **Rene Brun and Fons Rademakers** ROOT - An Object Oriented Data Analysis Framework, `https://root.cern/`

[23] **GSI Helmholtzzentrum für Schwerionenforschung GmbH** Go4, `https://www.gsi.de/en/work/research/experiment_electronics/data_processing/data_analysis/the_go4_home_page`

[24] **NIST** U.S Departement of Commerce `https://physics.nist.gov/PhysRefData/Star/Text/ESTAR.html`